communications biology

A Nature Portfolio journal

Article

Article in Press

https://doi.org/10.1038/s42003-026-11197-6

Altered developmental profile of the head-direction signal in a rat model of fragile X syndrome

Check for updates

Noah Moore[1,6], Adrian J. Duszkiewicz[2,3,4,6] ✉, Antonis Asiminas[1,5], Paul A. Dudchenko[2], Adrien Peyrache[3] ✉ & Emma R. Wood[1] ✉

Fragile X Syndrome is a common inherited, monogenic cause of intellectual disability and autism spectrum disorder, but the altered neural mechanisms underlying it remain unclear. Here, we investigate the development of the head-direction system in a rat model of Fragile X Syndrome (*Fmr1*$^{-/y}$ rats) through electrophysiological recordings in the postsubiculum during exploration and sleep. Surprisingly, juvenile *Fmr1*$^{-/y}$ rats exhibited sharper head-direction tuning and increased stability of the head-direction signal in relation to the external environment. Increase in intrinsic head-direction tuning persisted across behavioral and sleep states. In contrast, in adult *Fmr1*$^{-/y}$ rats, head-direction tuning was less stable than in wild-type rats despite normal intrinsic head-direction tuning. These findings suggest a transient sharpening of head-direction coding in juvenile *Fmr1*$^{-/y}$ rats, followed by a degradation in adulthood, mirroring the developmental regression often observed in neurodevelopmental conditions including Fragile X Syndrome. Overall, our work reveals systems-level dysfunctions in a rat model of Fragile X Syndrome and their developmental trajectories.

Autism spectrum disorder and intellectual disability (ASD/ID) are comorbid conditions characterized by abnormalities in early cognitive development that persist into adulthood. In many cases, their symptoms are linked to de novo or inherited mutations in genes involved in neuronal function[1]. With the aid of genetic rodent models, much progress has been made in uncovering how these single-gene mutations affect intracellular processes like excitability, synaptic transmission and plasticity[2]. However, how such synaptic phenotypes give rise to cognitive symptoms in ASD/ID at a systems level is not well understood.

The neurodevelopmental nature of ASD/ID necessitates quantification of systems-level phenotypes during early postnatal development—a task aided by the recent introduction of rat ASD/ID models[3–8]. Indeed, compensation mechanisms that emerge throughout adolescence often occlude the primary circuit dysfunctions that give rise to ASD/ID phenotypes[9]. In recent years, the problem has been addressed by focusing on primary sensory systems[10–12], in which neural tuning to sensory features can be quantified even in early postnatal development[13–15]. However, neural activity in sensory systems is principally driven by external stimuli and is thus sensitive to aberrations in upstream sensory processing as well as attentional control, each of which may also be affected in ASD/ID[16,17]. These different influences highlight the need to develop new paradigms to accurately assess the functional properties of cognitive circuits in juvenile rat models of ASD/ID, both when such activity is driven by and when it is independent of external stimuli.

In contrast to primary sensory systems, neurons in cortical networks that give rise to the brain's cognitive map often exhibit narrow tuning related to the animal's current position in space[18]. This spatial selectivity enables detailed mapping of their receptive fields in juvenile rats engaged in simple spatial exploration[19–22]. Importantly, neural activity in these networks is constrained to low-dimensional neural manifolds that persist across online (e.g., awake) and offline (e.g., sleep) states[23,24]. Recent work has shown that such manifolds provide access to neuronal tuning independently of the stimulus space[23–27], which makes these circuits ideal candidate model systems to study early postnatal network development in vivo.

The rodent head-direction (HD) circuit is a canonical example of a low-dimensional neural system in which population activity represents a one-dimensional circular variable[28]. In the awake state, this latent variable corresponds to the animal's current HD in the allocentric reference frame,

[1]Centre for Discovery Brain Sciences & Simons Initiative for the Developing Brain, University of Edinburgh, Edinburgh, UK. [2]School of Psychology, University of Stirling, Stirling, UK. [3]Montreal Neurological Institute and Hospital, McGill University, Montreal, Canada. [4]Division of Neuroscience, School of Biological Sciences, Faculty of Biology, Medicine and Health, University of Manchester, Manchester, UK. [5]Center for Translational Neuromedicine, Faculty of Health and Medical Sciences, University of Copenhagen, Copenhagen, Denmark. [6]These authors contributed equally: Noah Moore, Adrian J. Duszkiewicz.
✉e-mail: adrian.duszkiewicz@manchester.ac.uk; adrien.peyrache@mcgill.ca; emma.wood@ed.ac.uk

while during sleep it drifts and no longer relates to the external world[23]. This invariance of network topology across brain states indicates rigid functional connectivity, which can be probed by examining the neural manifold and the inferred latent state.

Here, we show that in a rat model of Fragile X Syndrome (FXS), an inherited monogenic cause of ASD/ID[29], the cortical HD signal is transiently sharper early in postnatal development but becomes unstable by adulthood. Using manifold analysis across online and offline brain states, we establish that the juvenile increase in sharpness is largely due to differences in intrinsic dynamics, while deterioration during adulthood stems from the difficulty with anchoring the HD signal to the external world. Overall, we introduce the rodent HD circuit as a valid and tractable model system that allows for unprecedented insights into network-level phenotypes in rodent models of neurodevelopmental disorders.

Results

We recorded populations of neurons in the postsubiculum (PoSub), the cortical hub of the HD system[30], in juvenile post-weaning (P22–28) male rats missing the only copy of the *FMR1* gene (*Fmr1*$^{-/y}$ rats; $n = 372$ units in 5 rats) as well as in their wild-type (WT) littermates ($n = 406$ units in 7 rats). PoSub cells were recorded using silicon probes (Figs. 1a and S1a, b) while rats foraged in an open field. Each recording day consisted of two 20 min foraging sessions, with a 90 min period of rest between sessions, during which sleep activity was recorded. Juvenile *Fmr1*$^{-/y}$ rats exhibited similar linear speed and angular head velocity as their WT littermates (Fig. S1c, d) and spent a similar amount of time facing the polarizing visual landmark (Fig. S1e). Our planned analyses focused on two complementary properties of the HD representation: the precision of HD tuning and the stability of the HD signal relative to the allocentric reference frame.

Statistical comparisons of cell-level data were performed using linear mixed-effects (LME) models to account for the hierarchical structure of cells nested within animals.

Excitatory cells in PoSub are tuned to HD in both adult and post-weaning juvenile WT rats[21,31], so we limited our analysis to well-isolated units of this putative cell type, using trough-to-peak duration as the classification criterion (Fig. S2a; range: 6–83 putative excitatory units per recording). While we observed directional tuning of putative excitatory cells in PoSub (henceforth referred to as PoSub cells) in both WT and *Fmr1*$^{-/y}$ juvenile rats, to our surprise well-tuned HD cells constituted a larger proportion of the recorded cell population in the latter (Fig. 1b–d). Quantification of HD tuning using either via HD information ("HD info") or the width of the tuning curves (Figs. 1e, f and S2e, f) confirmed that overall, PoSub cells in juvenile *Fmr1*$^{-/y}$ rats were indeed more sharply tuned to HD than PoSub cells in their WT littermates. This difference in tuning could not be explained by differences in cluster quality, firing rates, electrode positions or age at the time of recording (Figs. S2b–d and S2g, h).

The narrower HD tuning curves observed in juvenile *Fmr1*$^{-/y}$ PoSub cells could reflect either intrinsically sharper HD tuning or improved anchoring of the HD signal to the allocentric reference frame. To distinguish between these possibilities, we first compared HD tuning curves computed separately for the first and second half of each foraging session (Fig. 1g). While both genotypes showed sharper tuning computed for half of the session in comparison with the whole session, this improvement was larger in WT rats than in *Fmr1*$^{-/y}$ rats (Fig. S2j), pointing towards reduced HD signal drift in juvenile *Fmr1*$^{-/y}$ rats. We next quantified the angular drift of HD tuning curves between the first and second halves of the session, relative to the external reference frame. Indeed, despite overall stability across recording sessions (Fig. S2k), tuning curves in juvenile *Fmr1*$^{-/y}$ rats drifted less within each session than those of WT rats (Fig. 1h). This difference in drift was also observed on the population level (Fig. 1i, j). Thus, the apparent sharper HD tuning in juvenile *Fmr1*$^{-/y}$ rats could be explained, at least in part, by the lower degree of drift of the HD signal with respect to the allocentric reference frame.

If differences in anchoring to the external world underlie the differences in HD tuning, we would expect the overall HD tuning in juvenile *Fmr1*$^{-/y}$ rats to be similar to that of WT rats if computed independently of the allocentric reference frame. In other words, the fidelity of the internally generated HD signal should be the same across the two groups, with the differences lying in how this internal HD signal relates to the animal's real HD with respect to the environment. Highly structured intrinsic dynamics within the HD circuit enable estimation of relative HD tuning curves from population activity alone, independent of any external variables and reference frames[23]. We thus applied the Isomap dimensionality reduction technique to the PoSub cell population vectors obtained during the exploration sessions (Figs. S3 and S4a–c). In both WT and *Fmr1*$^{-/y}$ rats, the radial coordinate of PoSub population activity projected onto two dimensions corresponded to the animal's current HD and could be used to compute intrinsic ("manifold") HD tuning curves (Fig. 2a, b, e). However, while HD tuning curves reconstructed from the manifold corresponded well to the HD tuning curves calculated in the allocentric reference frame (Fig. 2c, d, f), these intrinsic tuning curves were better tuned to HD in juvenile *Fmr1*$^{-/y}$ rats than in their WT littermates (Figs. 2g and S4b, c). Thus, PoSub cells in juvenile *Fmr1*$^{-/y}$ rats exhibit intrinsically sharper tuning to HD independently of the possible differences in anchoring to the allocentric reference frame.

While the manifold HD obtained from population activity during wake periods should be independent of drift relative to the external environment, it is still conceivable that it is influenced by ongoing behaviour, sensory sampling, or state-dependent modulation. We therefore asked whether sharper intrinsic HD tuning in juvenile *Fmr1*$^{-/y}$ rats was also present during sleep (Fig. S4a and d), when HD population activity is internally generated in absence of consciousness and the HD signal, while coherent, is disengaged from the animal's current HD. We focused on Rapid Eye Movement (REM) sleep because HD cell population dynamics during this state closely resemble wakefulness[23,28]. In contrast to non-REM (NREM) sleep[32,33], the HD signal during REM is continuously expressed and drifts at approximately real-time speed, allowing tuning curves to be reconstructed using temporal binning comparable to wake exploration[23,25,28] (Fig. 3a, b). We found that, overall, juvenile *Fmr1*$^{-/y}$ rats had shorter REM episodes and spent a smaller proportion of sleep in REM (Figs. 3c and S4b, c), but the REM spiking activity was similar to wakefulness in both groups (Fig. S4e). HD tuning curves generated from the REM manifolds (Fig. S4d) corresponded well to the HD tuning curves calculated in the allocentric reference frame during exploration but were free from drift (Figs. 3d and S4b, c). Importantly, PoSub cells in juvenile *Fmr1*$^{-/y}$ rats still showed sharper HD tuning even when the tuning was computed from internally generated activity during REM sleep (Fig. 3e). Overall, these findings indicate that on top of enhanced anchoring to the allocentric reference frame, HD tuning in juvenile *Fmr1*$^{-/y}$ rats is intrinsically more precise.

We then sought to establish whether the increased sharpness of PoSub HD cell tuning in juvenile *Fmr1*$^{-/y}$ rats is transient or persists to adulthood. To that end, we recorded PoSub activity in adult *Fmr1*$^{-/y}$ rats ($n = 372$ units from 6 rats) and their WT littermates ($n = 406$ units from 6 rats) in the same experimental protocol (range: 30–114 putative excitatory units per recording; Figs. 4a, S6, and S7a–d). Since action potentials in adult rats tend to be narrower than in juveniles[34], we used a higher trough-to-peak threshold for identifying putative excitatory cells (Fig. S7a). In contrast to what we observed in juvenile rats, HD tuning in adult *Fmr1*$^{-/y}$ rats was no different than that of WT littermates (Figs. 4b–f and S7e–g). Analyzing both age cohorts together revealed that the sharpening of HD tuning was age-dependent (HD info, LME: age × genotype interaction, $\beta = -0.82$, 95% CI = [−1.50, −0.14], $\chi^2(1) = 4.98$, $p = 0.026$; n = juvenile WT: 7 rats/325 cells, juvenile *Fmr1*$^{-/y}$: 5 rats/245 cells, adult WT: 6 rats/398 cells, adult *Fmr1*$^{-/y}$: 6 rats/339 cells). However, while juvenile *Fmr1*$^{-/y}$ rats showed evidence of superior anchoring of the HD signal to the external world, adult *Fmr1*$^{-/y}$ rats showed an inverse phenotype, with more drift of the HD signal (Figs. 4g–j and S4h, i; tuning curve offset, LME: age × genotype interaction, $\beta = 0.88$, 95% CI = [0.21, 1.55], $\chi^2(1) = 5.86$, $p = 0.015$;

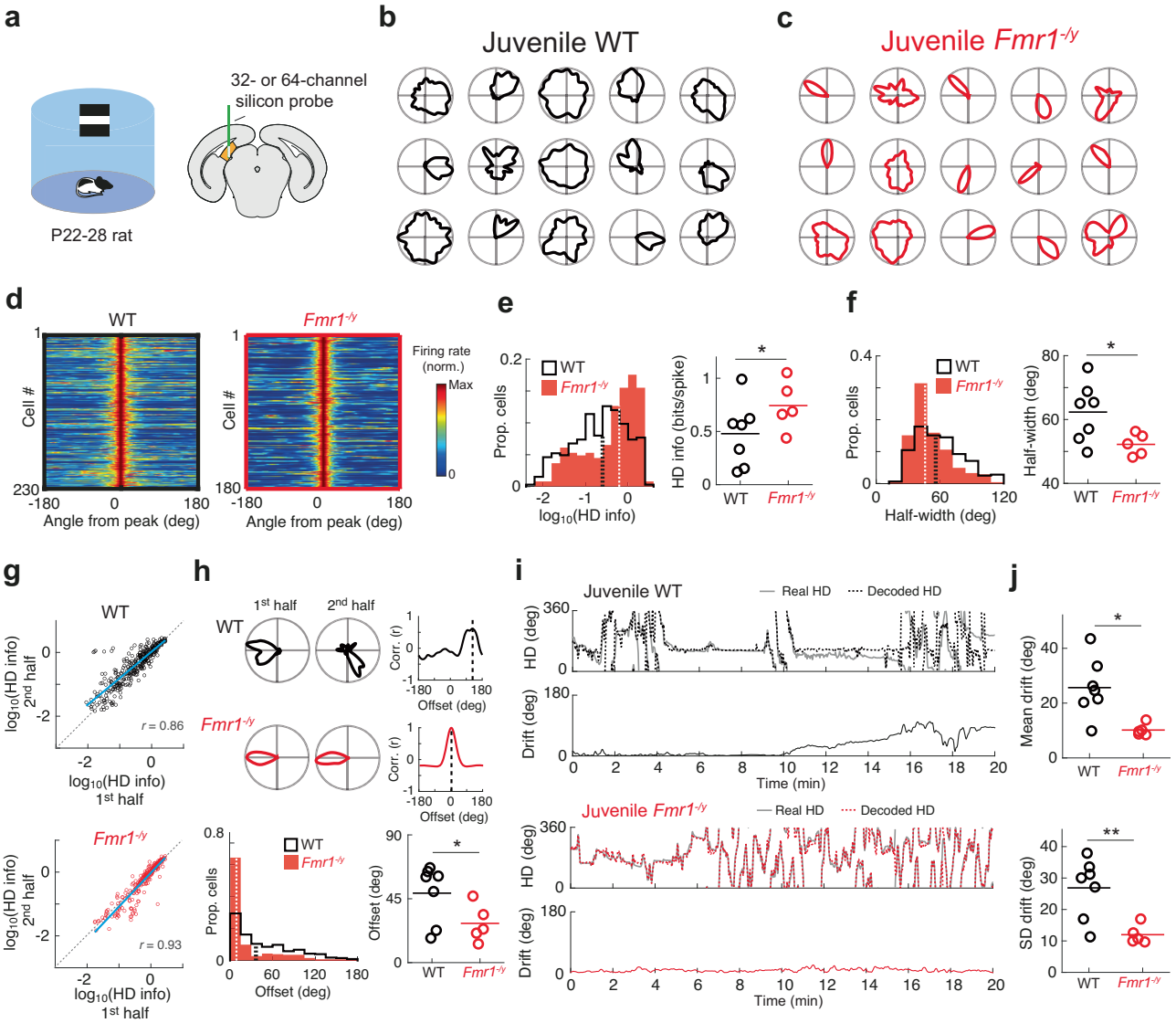


Fig. 1 | Sharper HD tuning and HD signal stability in juvenile *Fmr1*$^{-/y}$ rats. **a** Recording enclosure and silicon probe placement in PoSub. **b**, **c** Example tuning curves of a subset of PoSub cells in a juvenile WT rat (**b**) and a juvenile *Fmr1*$^{-/y}$ rat (**c**). **d** Normalized HD tuning curves of all PoSub cells with tuning curve width < 120°. **e**, **f** Overall distribution (left) and animal averages (right) of HD info (**e**) and tuning curve width (**f**) indicate sharper HD tuning in juvenile *Fmr1*$^{-/y}$ rats (HD info, LME, likelihood-ratio χ^2 test (two-sided): genotype effect, $\beta = 0.63$, 95% CI = [0.06, 1.19], $\chi^2(1) = 3.97$, $P = 0.046$; n = WT: 7 rats/325 cells, *Fmr1*$^{-/y}$: 5 rats/245 cells; half-width, LME, likelihood-ratio χ^2 test (two-sided): genotype effect, $\beta = -0.14$, 95% CI = [−0.27, −0.02], $\chi^2(1) = 4.52$, $P = 0.033$; n = WT: 7 rats/250 cells, *Fmr1*$^{-/y}$: 5 rats/207 cells). For tuning curve width, only cells with width < 120° were included. **g** Relationship between HD tuning of PoSub cells across two halves of the exploration epoch (WT, $r = 0.86$, $n = 325$, $P = 10^{-97}$; *Fmr1*$^{-/y}$, $r = 0.93$, $n = 244$, $P = 10^{-107}$). Blue lines, linear fits. **h** Top, examples of HD tuning curves for two halves of a recording epoch and associated tuning cross-correlograms, showing considerable drift in a PoSub cell from a WT rat but a stable firing direction in a cell from an *Fmr1*$^{-/y}$ rat. Dashed lines, angular offset of maximum tuning curve correlation. Bottom, distribution of tuning curve offsets between two halves of the exploration epoch for all cells, as well as animal averages, indicating enhanced anchoring (i.e., smaller offsets) of the HD signal to the allocentric reference frame in *Fmr1*$^{-/y}$ rats (LME, likelihood-ratio χ^2 test (two-sided): genotype effect, $\beta = -0.59$, 95% CI = [−1.12, −0.06], $\chi^2(1) = 3.97$, $P = 0.046$; n = WT: 7 rats/325 cells, *Fmr1*$^{-/y}$: 5 rats / 244 cells). **i** Example real and decoded HD during a single recording session in WT and *Fmr1*$^{-/y}$ rats, as well as the drift of the decoded HD with respect to the animal's real HD. **j** Juvenile *Fmr1*$^{-/y}$ rats show less drift of the HD signal within the recording session (two-sided Student's t-test on animal averages: mean drift, $t(10) = -3.13$, $P = 0.0106$, 95% CI = [−26.3, −4.45]; Standard deviation (SD) of drift, $t(10) = -3.32$, $P = 0.008$, 95% CI = [−24.6, −4.85]). Dashed lines on histograms, population medians; horizontal lines on animal average panels, means of animal averages. * $P < 0.05$, ** $P < 0.01$.

n = juvenile WT: 7 rats/325 cells, juvenile *Fmr1*$^{-/y}$: 5 rats/244 cells, adult WT: 6 rats/398 cells, adult *Fmr1*$^{-/y}$: 6 rats/339 cells; mean decoding drift, 2 × 2 ANOVA: age × genotype interaction, $F(1,20) = 19.33$, $n = 7$ WT juvenile, 5 *Fmr1*$^{-/y}$ juvenile, 6 WT adult, 6 *Fmr1*$^{-/y}$ adult rats, $p = 0.0002$; SD decoding drift, 2 × 2 ANOVA: age × genotype interaction, $F(1,20) = 15.37$, $n = 7$ WT juvenile, 5 *Fmr1*$^{-/y}$ juvenile, 6 WT adult, 6 *Fmr1*$^{-/y}$ adult rats, $p = 0.0008$).

As expected, the internal HD generated from the manifolds (Figs. S8a and Fig. 5e) matched real HD well (Fig. 5a–d, f) and there were no differences in the tuning of HD tuning curves obtained from the manifolds during periods of wakefulness (Fig. 5g) or REM sleep (Figs. 6a, b, d, e and S6d–i). Unlike juveniles, adult *Fmr1*$^{-/y}$ rats had WT-like duration of REM bouts (Figs. 6c and S9), indicating that this sleep phenotype was not present in adulthood.

Thus, the sharper quality of the intrinsic HD tuning curves in *Fmr1*$^{-/y}$ rats is developmentally transient and disappears as the rats reach adulthood. Furthermore, while juvenile *Fmr1*$^{-/y}$ rats displayed precise anchoring of the

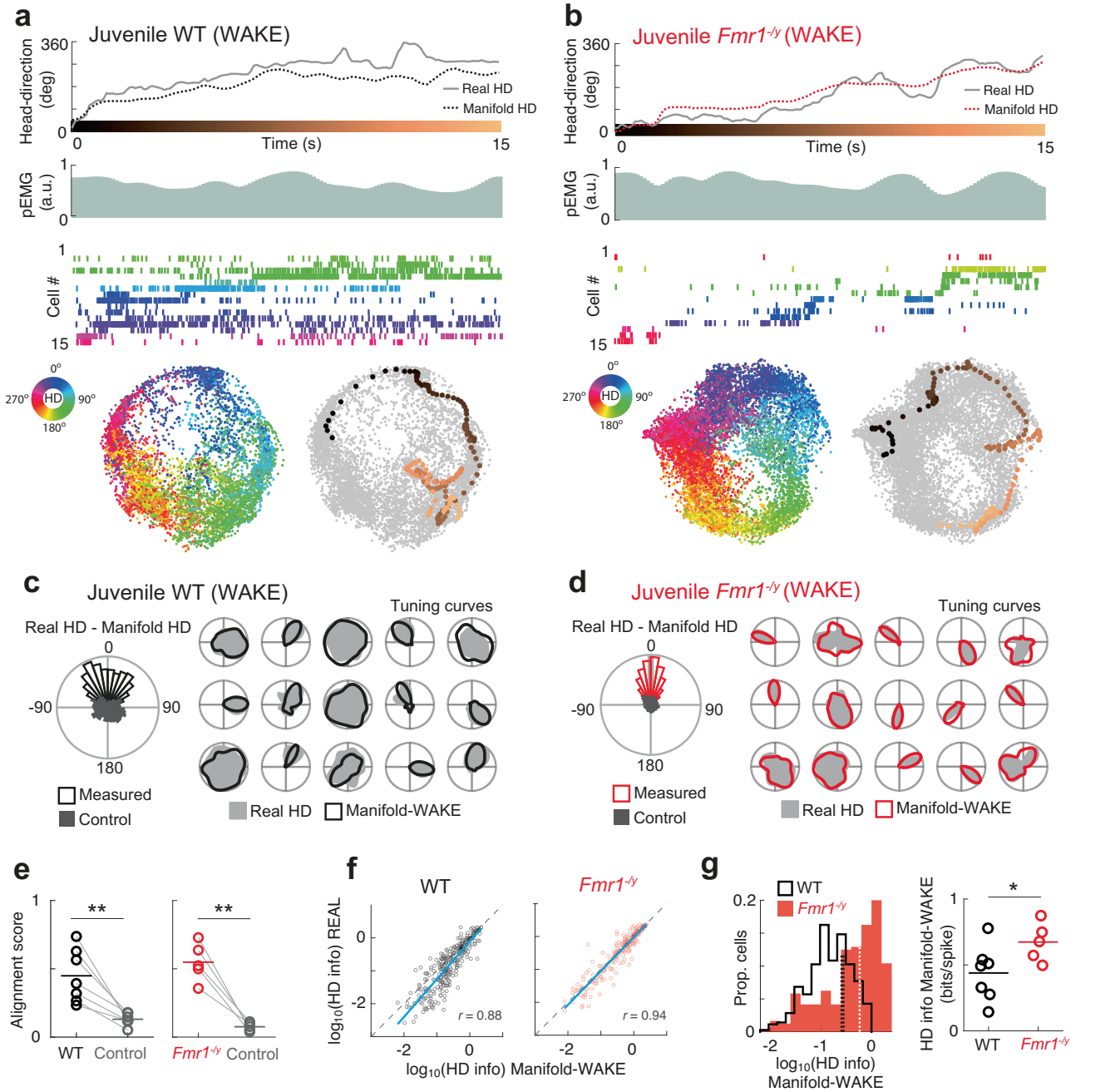


Fig. 2 | PoSub cells in juvenile *Fmr1*$^{-/y}$ rats show sharper tuning to the internal HD signal during wakefulness. a, **b** Examples of internal HD (top) decoded from Isomap projections (bottom) of PoSub cell spiking (middle, 15 cells with highest HD info) during a single awake exploration session (WAKE) in a juvenile WT rat (**a**) and an *Fmr1*$^{-/y}$ rat (**b**), with each population vector colored according to the animal's current HD. pEMG pseudo-electromyogram. **c**, **d** Alignment of the internal HD (angle from the centre of the manifold) to the real HD measured externally (left) and example HD tuning curves computed in the allocentric reference frame (Real HD) and reconstructed using the angle from the centre of the manifold (Manifold-WAKE). **e** In all animals alignment of the internal HD with real HD was stronger than in the control alignment computed by reversing the manifold angle in time (two-sided Student's *t*-test on animal averages: $t(6) = 4.60$, $n = 7$ rats, $P = 0.004$, 95% CI = [0.15, 0.49]; *Fmr1*$^{-/y}$: $t(4) = 6.76$, $n = 5$ rats, $P = 0.003$, 95% CI = [0.28, 0.67]). **f** Magnitude of HD tuning in PoSub cells is preserved in the tuning curves reconstructed only from the manifold during WAKE (WT, $r = 0.88$, $n = 325$ cells, $P = 10^{-104}$; *Fmr1*$^{-/y}$, $r = 0.94$, $n = 240$ cells, $P = 10^{-114}$). Blue lines indicate linear fits. **g** Overall distribution (left) and animal averages (right) of HD info indicate sharper tuning to internal HD in juvenile *Fmr1*$^{-/y}$ rats (LME, likelihood-ratio χ^2 test (two-sided): genotype effect, $\beta = 0.53$, 95% CI = [0.05, 1.01], $\chi^2(1) = 3.93$, $P = 0.047$; n = WT: 7 rats/325 cells, *Fmr1*$^{-/y}$: 5 rats/240 cells). Dashed lines on the histogram indicate population medians; horizontal lines on animal average panels are means of animal averages.* $P < 0.05$, ** $P < 0.01$.

HD signal to the allocentric reference frame, it degraded by adulthood despite intact intrinsic HD tuning.

Discussion

In the present study, we assessed how neural representations of the outside world are altered in a rat model of FXS. We leveraged the experimental tractability of the cortical HD system in *Fmr1*$^{-/y}$ rats to reveal unexpectedly sharper HD tuning in PoSub that is apparent in 3–4 week old juveniles but absent in the adult cohort. This phenotype was accompanied by an enhanced anchoring of the HD signal to the external world in juvenile *Fmr1*$^{-/y}$ rats, but reconstruction of the intrinsic HD tuning curves from PoSub cell activity manifolds during both wakefulness and REM sleep

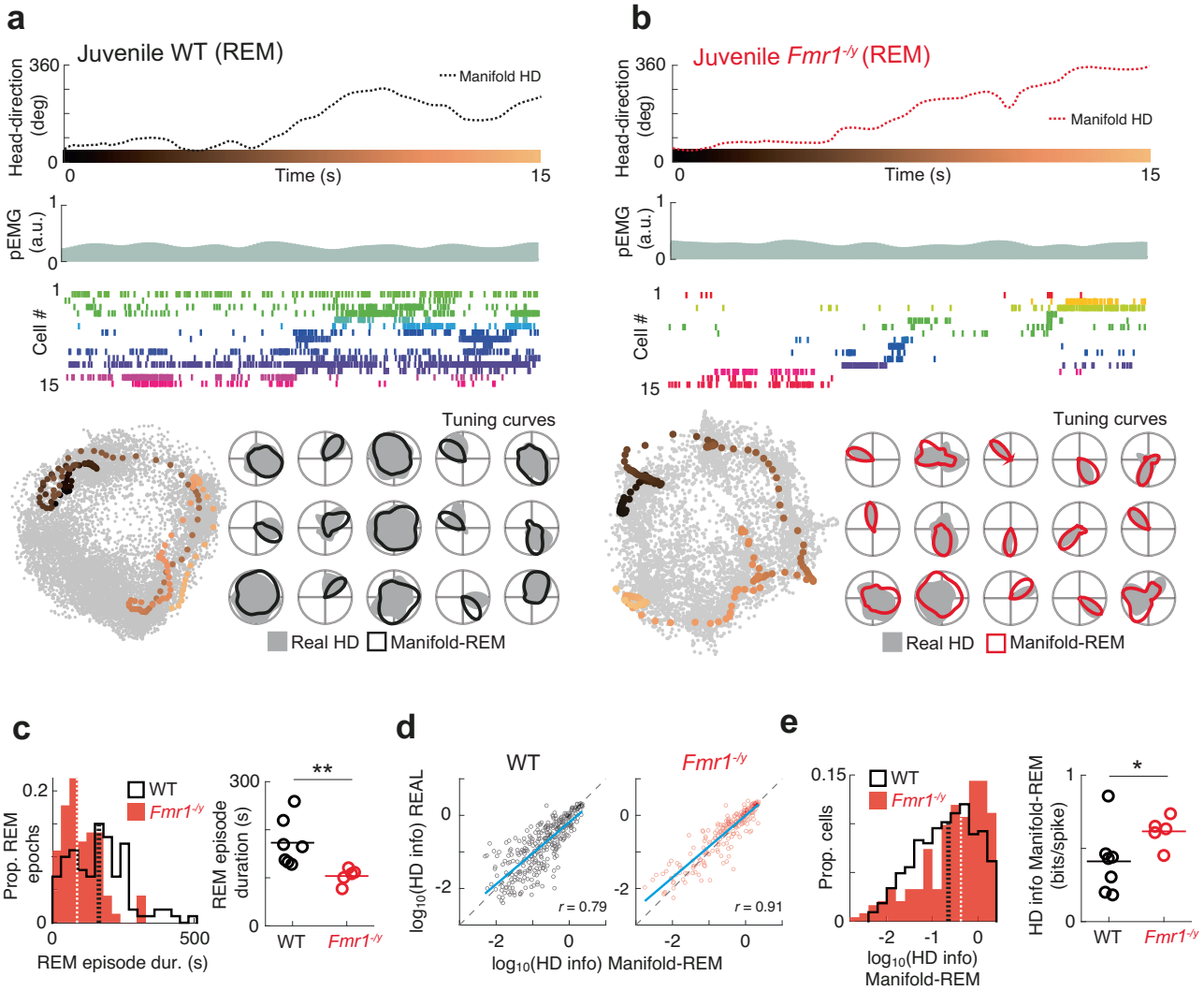


Fig. 3 | Sharper PoSub cell tuning to the internal head direction signal in juvenile *Fmr1*$^{-/y}$ rats persists during REM sleep. a, **b** Examples of internal HD (top) decoded from Isomap projections (bottom left) of PoSub spiking activity (middle) during REM sleep from the same recording session as in Fig. 2a–d. HD tuning curves (bottom right) can be reliably reconstructed from the REM sleep activity (Manifold-REM). **c** Juvenile *Fmr1*$^{-/y}$ rats have shorter REM episodes (LME, likelihood-ratio χ^2 test (two-sided): genotype effect, $\beta = -0.45$, 95% CI = [−0.75,−0.17], $\chi^2(1) = 6.73$, $P = 0.0095$; n = WT: 7 rats/100 episodes, *Fmr1*$^{-/y}$: 5 rats/75 episodes). **d** Magnitude of HD tuning in PoSub cells is preserved in the manifold REM tuning curves in both genotypes (WT, $r = 0.79$, $P = 10^{-79}$, $n = 325$ cells; *Fmr1*$^{-/y}$, $r = 0.91$, $n = 243$ cells, $P = 10^{-95}$). Blue lines, linear fits. **e** Overall distribution (left) and animal averages (right) of HD info indicate sharper HD tuning to internally generated activity during REM in juvenile *Fmr1*$^{-/y}$ rats (LME, likelihood-ratio χ^2 test (two-sided): genotype effect, $\beta = 0.51$, 95% CI = [0.07, 0.96], $\chi^2(1) = 4.78$, $P = 0.036$; n = WT: 7 rats/325 cells, *Fmr1*$^{-/y}$: 5 rats/243 cells). Dashed lines on histograms, population medians; horizontal lines on animal average panels, means of animal averages. * $P < 0.05$, ** $P < 0.01$.

allowed us to show that the increased sharpness of the HD signal in juvenile *Fmr1*$^{-/y}$ rats was independent of anchoring. In adult *Fmr1*$^{-/y}$ rats, in contrast, the anchoring of the HD signal to external landmarks was weaker than that of WT rats. Although the juvenile and adult recordings were obtained from separate cross-sectional cohorts rather than longitudinally from the same animals, the opposing genotype effects observed at the two ages are consistent with an age-dependent change in this neural representation.

Previous spatial phenotypes reported in *Fmr1*$^{-/y}$ rats have been subtle and highly dependent on age, brain area, and experimental conditions. Impairments in spatial memory and cognition have been reported in *Fmr1*$^{-/y}$ rats, including slower and poorer performance in a Morris water maze task[35] and a deficit in object-place-context recognition memory[3,4], but both of these phenotypes were sensitive to conditions such as experimental age and the exact training paradigm. Within the hippocampus, *Fmr1*$^{-/y}$ neurons show reduced experience-dependent changes in activity[5]. Consistent with individuals with ASD, *Fmr1*$^{-/y}$ rats show differences in sensory processing compared to WT rats. This includes degraded responses to auditory stimuli[36], faster reaction times to sound and impaired temporal but enhanced spectral modulation of loudness, compared to control[37], hyperactivity in the juvenile visual cortex[38], and altered neurological and behavioural responses to almond odour[39]. Thus, the phenotypes reported here are consistent with a pattern of neuronal alterations in spatial cognition and sensory processing.

The sharper HD tuning in juvenile *Fmr1*$^{-/y}$ rats may arise locally within PoSub or be inherited from alterations earlier in the HD circuit. The HD signal is thought to originate in a network comprising the dorsal tegmental nucleus (DTN) and lateral mammillary nucleus (LMN), which projects via the anterior nucleus of the thalamus to PoSub[40,41]. Modelling[42–45] and lesion studies[46,47] indicate that directional firing fields of HD cells depend on highly structured connectivity within the DTN–LMN network, whereby cells coding for similar directions support each other while cells coding for opposite directions inhibit one another, likely via inhibitory interneurons. Such ring-attractor-like dynamics constrain HD population activity to a common state space across brain states, allowing a coherent HD signal to be

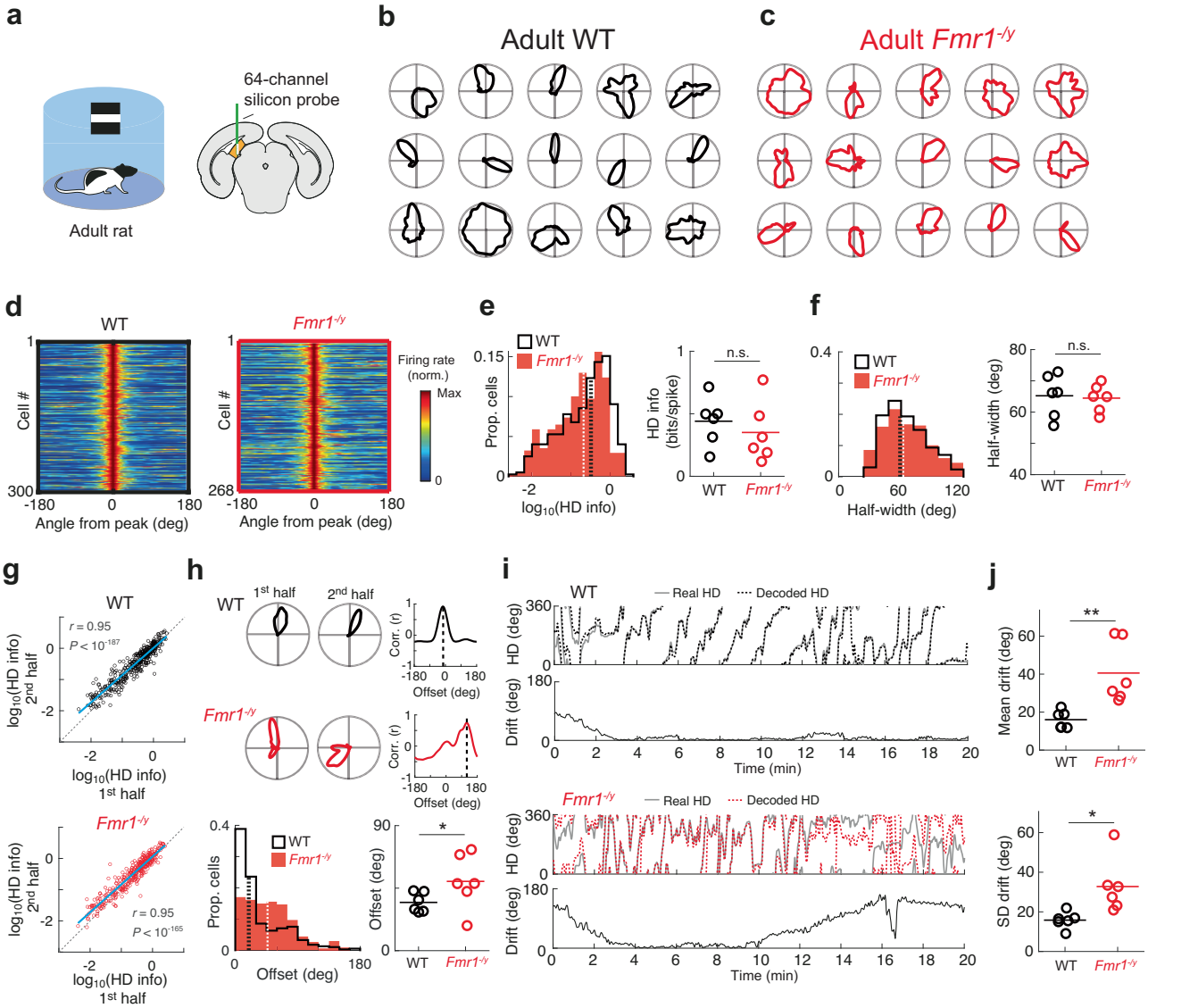


Fig. 4 | WT-like HD tuning but degraded HD signal stability in adult *Fmr1*$^{-/y}$ rats. **a** Recording enclosure and silicon probe placement in PoSub. **b**, **c** Example tuning curves of PoSub cells in adult WT (**b**) and *Fmr1*$^{-/y}$ rats (**c**). **d** Normalized HD tuning curves of PoSub cells with tuning curve width < 120°. **e**, **f** Overall distribution (left) and animal averages (right) of HD info (**e**) and tuning curve width (**f**) indicate normal levels of overall HD tuning non-directional in adults *Fmr1*$^{-/y}$ rats (HD info, LME, likelihood-ratio χ^2 test (): no genotype effect, $\beta = -0.19$, 95% CI = [−0.59, 0.21], $\chi^2(1) = 0.86$, $P = 0.35$; n = WT: 6 rats/398 cells, *Fmr1*$^{-/y}$: 5 rats/339 cells; half-width, LME, likelihood-ratio χ^2 test (two-sided): no genotype effect, $\beta = -0.011$, 95% CI = [−0.14, 0.12], $\chi^2(1) = 0.03$, $P = 0.87$; n = WT: 6 rats/300 cells, *Fmr1*$^{-/y}$: 6 rats/268 cells). **g** Degree of HD tuning in PoSub cell tuning curves is preserved between two halves of an exploration epoch, indicating stable tuning fidelity (WT, $r = 0.94$, $n = 398$ cells, $P = 10^{-188}$; *Fmr1*$^{-/y}$, $r = 0.95$, $P = 10^{-165}$). Blue lines indicate linear fits. **h** Top, examples of HD tuning curves for two halves of a recording epoch and associated tuning cross-correlograms, showing considerable drift in a PoSub cell from an *Fmr1*$^{-/y}$ rat but stable firing direction for a PoSub cell in a WT rat. Dashed lines indicate the angular offset of maximum tuning curve correlation. Bottom, overall distribution tuning curve offsets between two halves of the exploration epoch for all cells as well as animal averages (angular offset between tuning curves, LME, likelihood-ratio χ^2 test (two-sided): genotype effect, $\beta = 0.53$, 95% CI = [0.08, 0.97], $\chi^2(1) = 4.48$, $P = 0.034$; n = WT: 6 rats/398 cells, *Fmr1*$^{-/y}$: 6 rats/339 cells). **i** Example real and decoded HD during a single recording session in WT and *Fmr1*$^{-/y}$ rats, as well as the low-pass drift of the decoded HD with respect to the animal's real HD. **j** Adult *Fmr1*$^{-/y}$ rats show increased drift of the HD signal within the recording session (two-sided Student's t-test on animal averages: mean drift, $t(10) = 3.49$, $P = 0.006$, 95% CI = [8.75, 39.7]; SD drift, $t(10) = 2.89$, $P = 0.016$, 95% CI = [3.89, 30.0]). Dashed lines on histograms are population medians; horizontal lines on animal average panels indicate means of animal averages. * $P < 0.05$, ** $P < 0.01$. n.s. not significant.

decoded as a latent variable during sleep[25,28,33,48]. The tuning of individual HD cells is expected to depend on the effective connectivity within this circuit. Thus, one possibility is that the sharper cortical HD tuning observed in juvenile *Fmr1*$^{-/y}$ rats reflects altered connectivity or excitability within the upstream DTN–LMN circuit. Since DTN receives strong vestibular inputs conveying angular head velocity, one would predict accompanying changes in HD dynamics under conditions in which visual landmarks are removed, such as darkness, as well as possible changes in vestibular-dependent behaviours. Future experiments combining HD recordings with behavioural assays will be needed to determine whether the sharpened juvenile HD signal reflects improved or maladaptive circuit function.

An alternative possibility is that altered visual processing contributes to the juvenile phenotype. Although altered visual processing has, to our knowledge, not been directly characterized in *Fmr1*$^{-/y}$ rats, studies in *Fmr1*$^{-/y}$ mice show altered visual cortical function, including enhanced responses to low-intensity stimuli (Yang et al., 2022), degraded orientation tuning in primary visual cortex (Goel et al., 2018), and impairments in visual discrimination and other visually guided behaviours (Goel et al., 2018;

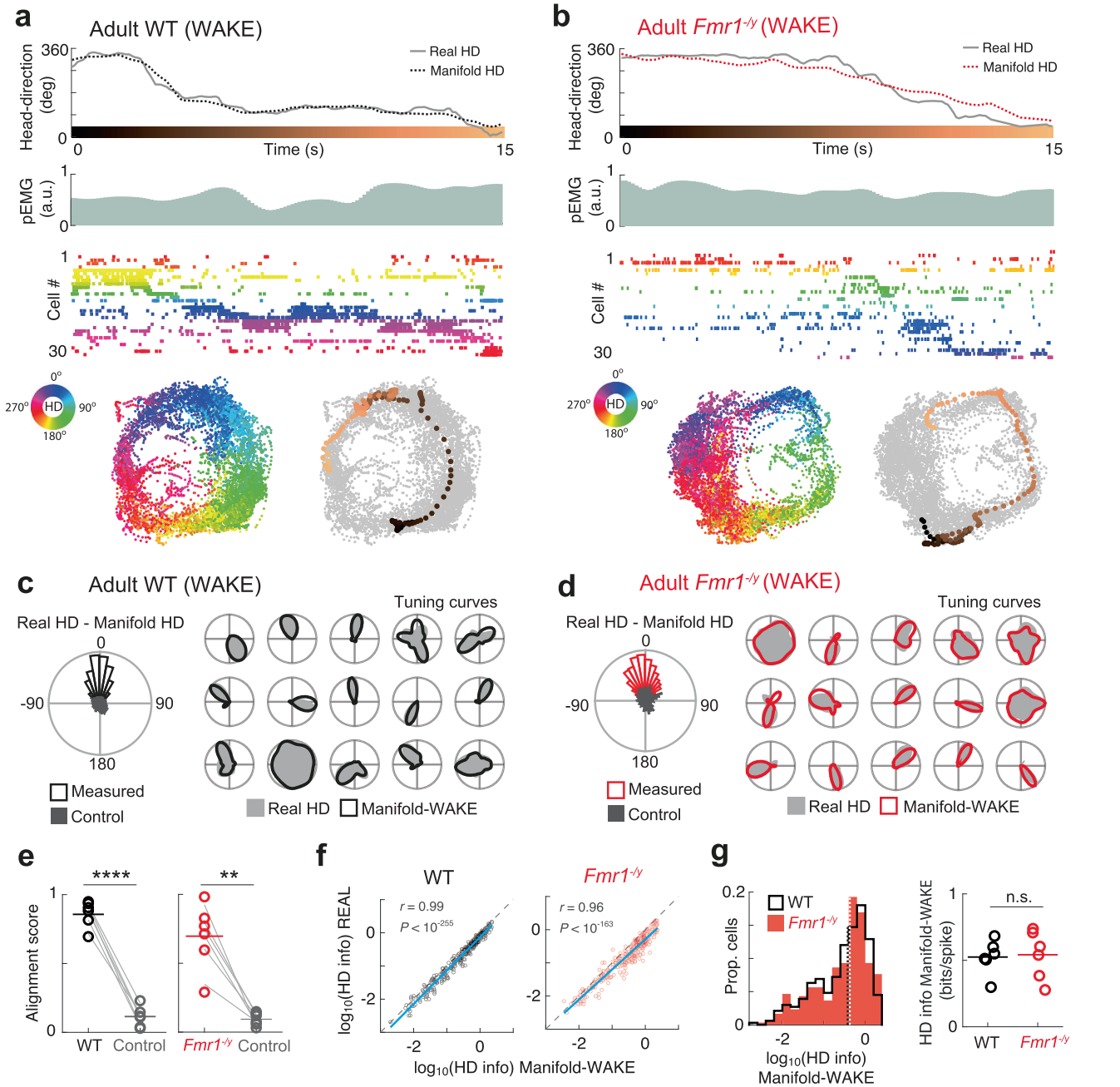


Fig. 5 | PoSub cells in adult *Fmr1*$^{-/y}$ rats show WT-like tuning to the internally generated HD signal during wakefulness. a, **b** Examples of internal HD (top) decoded from Isomap projections (bottom) of PoSub cell spiking (middle, 30 cells with highest HD info) during a single awake exploration session (WAKE) in an adult WT rat (**a**) and an *Fmr1*$^{-/y}$ rat (**b**), with each population vector colored according to the animal's current HD. pEMG pseudo-electromyogram. **c**, **d** Alignment of the internal HD (angle from the centre of the manifold) to the real HD measured externally (left) and example HD tuning curves computed in the allocentric reference frame (Real HD) and reconstructed using the angle from the centre of the manifold (Manifold-WAKE). **e** In all animals, alignment of the internal HD with real HD was stronger than in the control alignment computed by reversing the manifold angle in time (two-sided Student's *t*-test on animal averages, WT: $t(5) = 20.2$, $n = 6$ rats, $P = 5.5 \times 10^{-6}$, 95% CI = [0.65, 0.84]; *Fmr1*$^{-/y}$: $t(5) = 6.50$, $n = 6$ rats, $P = 0.0012$, 95% CI = [0.35, 0.81]). **f** HD tuning in PoSub cells is preserved in the tuning curves reconstructed from population activity during WAKE (two-sided Student's *t*-test on animal averages, WT, $r = 0.99$, $n = 397$ cells, $P = 10^{-316}$; *Fmr1*$^{-/y}$, $n = 339$ cells, $r = 0.96$, $P = 10^{-191}$). Blue lines indicate linear fits. **g** Overall distribution (left) and animal averages (right) of HD info indicate WT-like HD tuning in adult *Fmr1*$^{-/y}$ rats when measured independently of any reference frames (LME, likelihood-ratio χ^2 test (two-sided): no genotype effect, $\beta = 0.01$, 95% CI = [−0.31, 0.34], $\chi^2(1) = 0.006$, $P = 0.94$; n = WT: 6 rats/397 cells, *Fmr1*$^{-/y}$: 6 rats/339 cells). Dashed lines on histograms are population medians; horizontal lines on animal average panels indicate means of animal averages. ** $P < 0.01$, **** $P < 0.0001$. n.s. not significant.

Felgerolle et al., 2019). However, the sharper HD tuning observed in juvenile *Fmr1*$^{-/y}$ rats was also present when tuning was reconstructed from internally generated population activity during REM sleep, when ongoing visual sampling of the environment is absent. This makes it unlikely that the enhanced intrinsic HD tuning is simply a by-product of real-time altered visual input during exploration. Nevertheless, altered visual processing earlier in development may still have initiated downstream adaptations that affected PoSub function by the fourth postnatal week.

A related but distinct phenotype was the altered stability of the HD signal relative to the allocentric reference frame: juvenile *Fmr1*$^{-/y}$ rats showed reduced drift of the HD signal with respect to the environment, whereas adult *Fmr1*$^{-/y}$ rats showed increased drift despite intact intrinsic

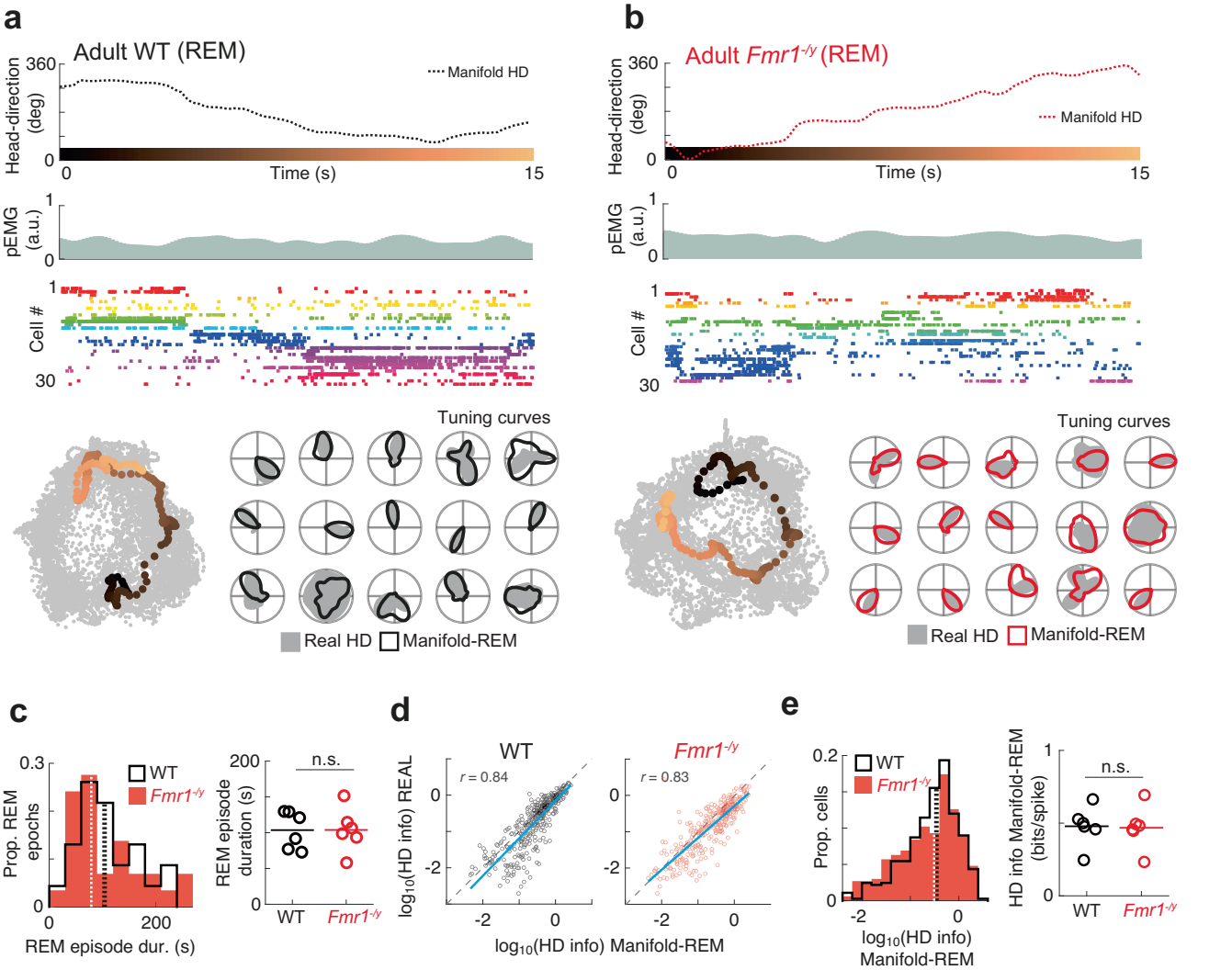


Fig. 6 | PoSub cells in adult *Fmr1*$^{-/y}$ rats show WT-like tuning to the internally generated HD signal during REM sleep. a, **b** Examples of internal HD (top) decoded from Isomap projections (bottom left) of PoSub spiking activity (middle) during REM sleep from the same recording session as in Fig. 5a–d. HD tuning curves (bottom right) can be reliably reconstructed from the REM sleep activity (Manifold-REM). **c** Adult *Fmr1*$^{-/y}$ rats have REM episodes of WT-like duration (LME, likelihood-ratio χ^2 test (two-sided): no genotype effect, $\beta = -0.01$, 95% CI = [−0.33, 0.36], $\chi^2(1) = 0.007$, $P = 0.94$; n = WT: 6 rats/23 episodes, *Fmr1*$^{-/y}$: 6 rats / 29 episodes). **d** Magnitude of HD tuning in PoSub cells is preserved in the manifold REM tuning curves in both genotypes (WT, $r = 0.83$, n = 367 cells, $P = 10^{-96}$; *Fmr1*$^{-/y}$, $r = 0.84$, $n = 333$ cells, $P = 10^{-89}$). Blue lines, linear fits. **e** Overall distribution (left) and animal averages (right) of HD info indicate WT-like HD tuning to internally generated activity during REM in adult *Fmr1*$^{-/y}$ rats (LME, likelihood-ratio χ^2 test (two-sided): no genotype effect, $\beta = -0.03$, 95% CI = [−0.38, 0.32], $\chi^2(1) = 0.028$, $P = 0.87$; n = WT: 6 rats/367 cells, *Fmr1*$^{-/y}$: 6 rats/333 cells). Dashed lines on histograms, population medians; horizontal lines on animal average panels, means of animal averages. n.s. not significant.

HD tuning. This dissociation suggests that intrinsic HD tuning and alignment to the external world can be altered independently, which is consistent with previous work showing that a coherent internal HD signal can persist even when it is not correctly anchored to the allocentric reference frame. For example, an internally organized but weakly anchored HD signal is present in very young rats before eye opening[22], and adult rodents show detachment of the HD signal from the external world when visual inputs are compromised[49]. In young rats, anchoring can be improved by providing somatosensory information through environmental borders, indicating that mapping the internal HD signal onto the external world is a multisensory process.

Anchoring of the HD signal is exceptionally stable in adulthood, with the specific mapping between the HD signal and the external environment persisting for weeks even after a single exposure[50]. The anchoring mechanism is likely to involve PoSub[51,52]. Vision is the primary modality for this process—anchoring of the HD signal is strongly controlled by visual landmarks[53–55] and visual landmark stimuli are known to refine the HD coding in PoSub[56]. The directional information about stable visual landmarks may reach PoSub either directly from the visual cortex, area 29e[57], or via prominent inputs from the retrosplenial cortex, where the activity of a fraction of neurons is selective for visual landmarks[58,59]. Our observations of altered allocentric stability of the HD signal in *Fmr1*$^{-/y}$ rats are consistent with altered processing in the pathway that conveys the visual information to the HD circuit, perhaps through altered visual gain control. However, a limitation of the present study is that differences in anchoring to the allocentric reference frame were inferred indirectly. Specifically, we quantified drift of the HD signal with respect to the recording environment and compared conventional HD tuning curves with tuning reconstructed from the intrinsic population manifold. These analyses distinguish intrinsic HD tuning from stability relative to the external frame, but they do not identify the specific external cues or internal sensory circuits controlling that stability.

An alternative interpretation is that the increased allocentric stability observed in juvenile *Fmr1*$^{-/y}$ rats does not necessarily reflect functionally superior anchoring. Instead, it may reflect a more rigid coupling of the HD signal to the current environmental reference frame, or reduced flexibility in updating the HD representation when external cues change. This interpretation is consistent with behavioural rigidity often observed in autism[60–62]. Because the visual landmark was held constant, the present experiments cannot determine whether reduced drift in juvenile *Fmr1*$^{-/y}$ rats reflects stronger adaptive anchoring or excessive rigidity. Future experiments using cue rotation, cue removal, darkness, or visual-vestibular conflict will be needed to test whether the juvenile phenotype reflects flexible stabilization of the HD signal or reduced responsiveness to changing external cues. Although our wake analyses were restricted to periods in which animals were actively moving, and we observed no clear genotype differences in linear or angular head velocity, animal-level relationships between these movement measures and HD tuning or drift were necessarily imprecise given the sample size. Behavioural variation therefore cannot be excluded as a contributing factor, although the persistence of sharper intrinsic HD tuning during REM sleep, when animals were immobile and not sampling the environment, indicates that waking movement statistics are unlikely to fully explain the juvenile HD tuning phenotype.

The systems-level phenotypes reported here must ultimately reflect changes in the cellular and synaptic properties of the HD circuit or of its sensory inputs. In FXS, loss of the *FMR1* gene prevents expression of fragile X messenger ribonucleoprotein (FMRP), an RNA-binding protein that regulates local protein synthesis and multiple aspects of neuronal function. However, the relationship between loss of FMRP and circuit-level function is unlikely to be simple or linear. In particular, the altered HD tuning and anchoring observed in *Fmr1*$^{-/y}$ rats may not reflect direct consequences of FMRP loss in PoSub or upstream HD regions alone, but may instead arise from developmental adaptations to earlier cellular or synaptic disturbances. For example, the hyperexcitability seen in the *Fmr1*$^{-/y}$ CA1 cells is associated with reduced functional inputs from the entorhinal cortex, meaning that it may result from adaptive or homeostatic regulation induced by reduced functional synaptic connectivity[63]. Using ex vivo electrophysiology and computational modelling, it was shown that an increased excitation/inhibition ratio in the *Fmr1*$^{-/y}$ mouse somatosensory cortex does not lead to changed firing rates downstream, because altered excitatory and inhibitory synaptic conductances counteract each other[64]. The result in vivo is a largely normal sensory tuning with a mildly blurred whisker map, suggesting that some of the changes in excitability seen in the animal models of FXS may be tuned to counterbalance the direct effects of the mutation and preserve network output.

This compensatory interpretation is also supported by evidence that some *Fmr1*$^{-/y}$ phenotypes emerge only later in development, rather than being present from the earliest stages of circuit function[11,64]. In support of the possibility of hyperexcitability arising secondary to previous phenotypes, in *Fmr1*$^{-/y}$ rats before eye-opening, visual cortical neurons have reduced spike rates, indicating hypoexcitability[65]. After the fourth postnatal week, mild hyperexcitability emerges as both an increase in both visually-evoked spiking[65] and high-frequency oscillations in the visual cortex during rest[65]. This may also explain why cellular and neuronal hyperexcitability is not found in every brain region and cell type, as each one may develop compensatory changes differently. This may be tied to the phenomenon of developmental regression, sometimes observed in children with autism, where already acquired skills are lost, usually around the 2nd and 3rd year of life[66]. The deficient anchoring of the HD signal to the external world, reported here, was only observed in adulthood, and therefore may arise as imperfect homeostatic adaptations to a lack of FMRP.

A distinct possibility is that the effects observed in this study are not solely due to altered cellular or synaptic properties within the HD circuit, but are partly mediated by broader differences in emotional or attentional regulation. Such an interpretation would be consistent with observations in people with FXS (Munir, Cornish and Wilding, 2000; Cohen et al., 2015) as well as reports of altered stress reactivity, arousal, and attentional engagement in Fmr1-knockout mice (Moon et al., 2006, 2008; Qin et al., 2011). Differences in these state-dependent variables could affect neural information processing through modulatory influences, producing changes in HD activity that are not specific to the HD circuit itself. Although our analyses of wakefulness epochs were limited to the times when animals were actively ambulating, we did not observe gross behavioural differences in linear or angular head velocity between genotypes, these measures provide only indirect evidence about internal behavioural state, and the present study was not designed to assess this possibility directly.

Finally, one of our incidental findings was that juvenile *Fmr1*$^{-/y}$ rats have more fragmented REM sleep. Juvenile rats have longer REM bouts compared to adults[67] and REM sleep is associated with learning[68] and may direct the course of brain maturation through the control of neural activity[69]. In the cortex, REM sleep is responsible for crucial developmental processes such as pruning and strengthening dendritic spines appropriately[70], and experimental suppression of REM sleep alters behavioural, anatomical, and biochemical development[69,71,72]. Sleep disruption has also been observed in Fmr1$^{-/y}$ mice, with studies reporting reduced sleep duration in adult animals[73,74]. This mouse phenotype appears to exhibit a developmental profile, with normal sleep duration at P21 but reduced sleep duration in adulthood[73]. In contrast, in the present study juvenile *Fmr1*$^{-/y}$ rats showed shorter REM bouts, while adult *Fmr1*$^{-/y}$ rats showed REM episode durations comparable to WT animals. Thus, rather than pointing to a uniform sleep deficit across development, these findings suggest that sleep phenotypes in FXS models are developmentally regulated and may manifest differently depending on age, species and the specific aspect of sleep architecture being measured.

Still, the finding of shorter REM bouts in juvenile *Fmr1*$^{-/y}$ rats is consistent with studies in human children with FXS, reporting disrupted sleep microstructure, less time in REM sleep, and frequent night awakenings[75], while more problematic health or behavioural characteristics were associated with higher likelihood of sleep problems[76]. Thus, a more fragmented sleep with shorter REM bouts, especially during development, can be both an effect of lack of FMRP and a cause for some of the intellectual disability-related phenotypes observed in *Fmr1* knockout animals and individuals with FXS.

Conclusions

In summary, in the current study we have shown that the head direction system is altered in *Fmr1*$^{-/y}$ rats. The nature of this alteration suggests an apparent early gain-of-function followed by a decline. This pattern is intriguing as it echoes developmental regression, in which children with FXS and other neurodevelopmental conditions may acquire certain cognitive skills early in life but later lose them. Additionally, while our focus here has been on the head direction cell system because of its tractability, the current results may imply alterations in other spatial representations in the brain, for example those provided by place cells and grid cells, which likewise provide internal representations of space that are anchored to external landmarks.

Methods

Animals

All experimental procedures were carried out under a UK Home Office project licence (PP5496934), approved by the Animal Welfare and Ethical Review Board of the University of Edinburgh, and conformed with the UK Animals (Scientific Procedures) Act 1986. Long-Evans male *Fmr1*$^{-/y}$ and WT rat littermates were bred in-house by crossing WT sires with *Fmr1*-heterozygous dams. The original null mutants were generated using zinc finger nucleases targeting *Fmr1* exon 1 with a construct containing the sequence coding for eGFP. The *Fmr1*$^{-/y}$ males from the resulting line do not express either FMRP or eGFP, as described by ref. 4. The rats used for the current experiments were bred in-house and were housed with their parents and siblings up until weaning (P21). After weaning, animals were housed in mixed genotype littermate cages. They were kept on a 12 h/12 h light/dark cycle (lights on at 7am) and fed *ad libitum* on standard laboratory chow, with supplementation of water-soaked breeding chow after the surgery.

Twenty-four hours after the end of the surgery, adult rats were placed on mild food restriction to encourage foraging, with their body weight not falling below 90% of their free feeding weight. Experiments in juvenile and adult rats were performed sequentially. Animals in both cohorts were bred from the same in-house colony, but juvenile and adult recordings were obtained from different litters. Within each litter, rats were randomly allocated to the experiment. Experimenters were blind to the genotype of the animals throughout experiments, including surgery, recordings, and pre-processing, and were unblinded for data analysis.

Surgery

Rats were anaesthetised using 1.5–3.5% isoflurane, while the animal's respiratory rate and heart rate were monitored using a PhysioSuite (Kent Scientific) and their body temperature was maintained at 37° using a homeothermic blanket system (Harvard Apparatus). 0.08 ml per kg body-weight of Rimadyl (50 mg/ml carprofen) was administered subcutaneously shortly after induction of anaesthesia. To secure the headcap and implant on the head, the skull was covered with dental adhesive (Optibond Universal). In adults, this was supplemented with three to five self-tapping jeweller's screws. A silver ground wire was placed through the craniotomy directly above the cerebellum in juveniles or attached to one of the skull screws placed above the cerebellum in adult rats. A craniotomy was drilled over the left PoSub, and a silicon probe (Cambridge Neurotech, models H5, H6b, or H7) was lowered into the brain, slightly above the target area (juveniles, from Bregma: anterior-posterior (AP), −6.30 mm; medial-lateral (ML), 3.10 mm; dorsal-ventral (DV), −1.60 mm; adults, from Bregma: AP, −7.64 mm; ML, 3.30 mm; DV, −1.70 mm). The silicon probe was mounted on a drive (3DNeuro or made in-house), secured onto the skull's surface using dental acrylic. After surgery, the animals were allowed to recover on a heated bench (30 °C) for at least one hour and returned to the animal house for at least 24 h before recording. Juvenile rats were single housed after surgery and adults were single-housed or housed with a sibling in a cage with a divider separating them. Juvenile rats were implanted between P20 and P23 and adult rats were at least 7 weeks old at the time of implantation.

Behavioural protocol and electrophysiological recording

The probes were initially implanted in the white matter above PoSub and were subsequently advanced slowly into PoSub (speed: 0.28 mm/h in 0.035 mm increments) 24–48 h after implantation. The tissue was allowed to settle for at least 3 h before recordings commenced. The recording environment consisted of a blue plastic cylindrical arena of 73 cm diameter, with 54 cm tall walls. A prominent visual cue card with vertical black and white stripes was positioned near the top of the wall. The rat was taken within the curtains surrounding the recording enclosure, plugged in and placed within the cylindrical arena from the side opposite to the visual cue and facing the cue itself. Cereals were then scattered on the floor and the rat was left to forage and explore for 20 min. After that, the rat was given a 90-min sleep opportunity in an opaque container placed inside the recording arena, during which recordings continued. The arena was swept and cleaned with chlorhexidine (Vetasept) spray between the exploration and sleep sessions.

For recording, the implanted silicon probe was connected to a head-stage (RHD, Intan technologies). The headstage was connected to an Intan RHD standard SPI cable, which was connected to a 3D-printed commutator in the ceiling (custom-made in house). Signal was acquired at 30 kHz with an OpenEphys data acquisition system. For tracking the rat's position and HD, a red and a green marker were attached on the right and left of the headstage. Video capturing and marker tracking were performed using Bonsai software[77] at 40 Hz. For the juvenile recordings, video images were acquired through a Logitech C930e camera. To synchronise the image with the electrophysiology data, an Arduino microcontroller was programmed to send a random sequence of pulses to both the OpenEphys system and a LED light within the frame of the camera. The times when the LED light was on were detected by Bonsai and synchronisation of the pulses in the light and the electrophysiology data was done offline. For the adult recordings, images were acquired through an acA1300-75gc Basler camera with a LMVZ4411 Kowa lens, positioned at the ceiling of the rig. This camera was connected to the OpenEphys board, sending a TTL pulse for each frame taken, allowing the synchronisation of the two streams of information.

Perfusion and probe recovery

After the end of data gathering, the rats were anaesthetised with 5% isoflurane and injected intraperitoneally with a lethal dose of pentobarbitone (≥ 1 ml for adults and ≥ 0.3 ml for juvenile rats). After their reflexes were gone, they underwent transcardial perfusion first with 0.9% saline, and then with 4% formalin or paraformaldehyde solution. The rat was then decapitated and the brain extracted. The probe and drive complex was carefully recovered from the headcap. After recovery, the probe was dipped in and out of a 1:5 solution of Contrad 70 liquid detergent in distilled water heated to roughly 60 °C for 5 minutes, twice. After that, the probe was left to soak in a 1–2% fresh solution of tergazyme detergent, and finally another round of dips in warm Contrad was performed. The probe was then rinsed with distilled water, and channel impedances were measured in 0.9% saline using the OpenEphys system. If the recording quality of the previous rat was good and the impedance values were satisfactory (most channels <0.5 MOhm), the probe was reimplanted in the next rat.

Behavioural analysis

Animal's HD was calculated from the relative x–y positions of the two headstage markers using the four-quadrant inverse tangent function, corrected by a constant offset between the lateral headstage axis into the animal's forward-facing direction. Animal's position was defined as the average x-y position of the two headstage markers. Linear velocity was calculated as the frame-to-frame Euclidean displacement of the tracked position divided by the inter-frame interval, and was smoothed with a 0.25 s moving average window. Angular head velocity (AHV) was calculated from the frame-to-frame circular difference in HD, divided by the median inter-frame interval and converted to degrees/s. For each recording epoch, mean linear velocity and mean absolute AHV were calculated during active exploration epochs, and values were then averaged across recordings. The egocentric cue bearing was computed by subtracting the animal's HD from the allocentric angle to the visual cue. Epochs in which the animal was facing the cue were defined as periods when the absolute egocentric cue bearing was within 90°, whereas epochs facing away from the cue were defined as periods when the absolute egocentric cue angle was greater than 90°.

Spike sorting and cell classification

Spikes were first split automatically into clusters using Kilosort 2.0 (Pachitariu et al., 2016). Manual curation was performed while visualising the automatically created clusters on Klusters software. At this stage, any cluster without a clear waveform and clear dip in the spike train autocorrelogram at the 0–1 ms time bin was classified as noise and cluster pairs with similar waveforms and a clear dip in their spike train cross-correlograms at the 0–1 ms time bin were merged. Viable units were first identified as units that had a waveform with negative deflection (criterion aiming to exclude spikes from fibers of passage). Next, a cluster contamination score was computed from the spike autocorrelograms, as a ratio of the amplitudes of the 0–1 ms bin and the maximum amplitude within 0–100 ms. Units with cluster contamination scores below 0.5 were excluded from the analysis. Next, putative excitatory cells were classified on the basis of trough-to-peak duration of their average waveforms. The threshold for classification was based on the trough of the bimodal distribution of trough-to-peak durations and was set at 0.5 ms for juvenile rats and 0.4 ms for adult rats. Finally, for each analysis, units with less than 100 spikes fired within the analyzed epoch were excluded.

HD tuning curves

The animal's HD was calculated based on the line perpendicular to the line connecting the red and green markers attached to the headcap. Periods with more than 1 s without viable tracking data were excluded from the analysis.

HD tuning curves were then computed as the mean firing rate of the cell in each angular bin. Tuning curves were calculated in bins of 1° (spikes/time) and smoothed with a Gaussian kernel of 6° SD. For Isomap analyses, tuning curves were computed in 6° bins (with 12° SD Gaussian kernel) to account for the relatively short duration of REM sleep episodes in adult rats. Speed was computed as the difference in the animal's position at successive time points and was smoothed with a moving average window of 0.25 s. HD tuning curves were computed from epochs when the animal's speed exceeded 1.5 cm/s.

Half-width of the HD tuning curves was computed by first finding the bin with the highest firing rate, and then averaging the two sides of the tuning curve. Half-width was then defined as twice the angular distance between the maximal firing rate and the half-maximal firing rate of the resulting half of the tuning curve. Cells without a clearly defined bump in their tuning curves (tuning curve width > 120° were excluded from analyses of tuning width. HD information contained in the tuning curves calculated for N angular bins as:

$$I = \sum_{i=1..N} \lambda(\Theta_i) log_2 \frac{\lambda(\Theta_i)}{\lambda} p(\Theta_i)$$

where $\lambda(\Theta_i)$ is the firing rate of the cell for the ith angular bin and λ is the average firing rate of the neuron during exploration. We used uniform occupancy $p(\Theta_i)$ to be able to compare tuning curve shapes irrespective of behavioural differences.

HD tuning curve cross-correlograms were obtained by computing Pearson's correlation coefficients between the reference tuning curve vector and the second tuning curve vector (from either the same or another cell), which was circularly shifted by 1 to maximum number of bins. Difference in HD information between tuning curves computed using different epochs was calculated as normalized difference between two scores, using the formula $(\text{HDinfo}_{\text{epoch2}} - \text{HDinfo}_{\text{epoch1}})/(\text{HDinfo}_{\text{epoch2}} + \text{HDinfo}_{\text{epoch1}})$.

Bayesian decoding and drift estimation

To estimate the degree of drift of the internal HD with respect to the allocentric reference frame, excitatory cell spike times were binned into population vectors (200 ms window, smoothed in 400 ms SD Gaussian windows). Based on cells' tuning curves from the baseline period (first half of a recording epoch), the population vectors were converted into a Bayesian probabilistic map under the hypothesis that HD cells fire as a Poisson process[78]. The instantaneous internal HDs were taken as the maxima of these probabilistic maps. The degree of drift of the HD signal was calculated as the decoder error: angular difference between the real HD and the decoded HD at each time bin. To obtain the slow drift signal, decoder error was denoised with a Hampel filter (5 s window, 1 SD) and then smoothed with a 0.8 s SD Gaussian window. The mean and SD of the decoding error was calculated from the second half of the recording session, restricted to times in which the animal's velocity exceeded 1.5 cm/s. Recording sessions with less than 6 putative excitatory cells that fired more than 100 spikes ($n = 1$ session) were excluded from this analysis.

Classification of sleep states

The wide-band signal was downsampled to 1.25 kHz and used as the local field potential (LFP) signal. Sleep scoring was performed using the automated SleepScoreMaster algorithm and TheStateEditor software (Buzsaki laboratory, https://github.com/buzsakilab)[79,80]. Briefly, the algorithm selected channels with strongest overall slow-wave activity (slope of the power spectrum between 4 and 90 Hz) and theta power (5–10 Hz) above the aperiodic component. It then computed slow-wave activity and theta-band power in a sliding window (2 s width, 50% overlap). Additionally, pseudo-electromyograph was computed by selecting four approximately equally spaced usable channels per shank, band-pass filtering the LFP signal (300–600 Hz) and computing the mean pairwise correlation between filtered.

Sleep states were then classified using a rule-based approach, with NREM identified by high slow-wave activity, REM by high theta activity during periods of low movement outside NREM, and all remaining periods classified as wakefulness. Thresholds for each feature were determined automatically as the minimum between the two dominant modes of the feature's histogram. All automatically scored recordings were subsequently inspected manually using TheStateEditor to verify the accuracy of state classification.

Visualization and analysis of the population manifold

For visualization and analysis of the PoSub population manifold, cell spike times from the whole epoch were binned into population vectors in 200 ms bins, smoothed with a Gaussian kernel of 400 ms SD, and square-root transformed. The resulting binned firing rates were z-scored in the time domain, and each population vector was normalized by dividing it by its L2 norm. Population vectors were restricted to epochs in which the animal's velocity exceeded 1.5 cm/s in juvenile rats or 3 cm/s in adult rats, and were then input into the Isometric Feature Mapping (Isomap) algorithm implemented in the Matlab Toolbox for Dimensionality Reduction (version 0.8.1b, https://lvdmaaten.github.io/drtoolbox/). The parameters were set to 25 nearest neighbours and 2 dimensions. Recording sessions with fewer than 6 putative excitatory cells that fired more than 100 spikes were excluded from this analysis.

This analysis was used to estimate the internally generated HD state from the geometry of population activity. Because HD population activity is organized as a ring, population vectors corresponding to similar internal HD states are expected to lie near one another on the manifold, whereas different internal HD states occupy different angular positions around the ring. Manifold HD at each time bin was therefore calculated as the four-quadrant arctangent of the two Isomap dimensions, yielding an angular coordinate ranging from −180° to 180°.

The manifold HD generated this way has arbitrary directionality, clockwise or anticlockwise, and an arbitrary point of origin. To align the manifold HD obtained during wakefulness with real HD, manifold directionality was first established by computing the correlation between unwrapped real and manifold HD values and multiplying the manifold HD values by −1 if the correlation was negative. Manifold HD was then aligned to real HD by computing the manifold offset as the circular mean of the difference between real and manifold HD, and circularly shifting all manifold HD values by this offset value. The alignment score was computed as the Rayleigh vector length of all offset values after alignment.

Manifold tuning curves were computed as the ratio between histograms of spike count and total time spent in each internal HD bin, using 6° bins, and were smoothed with a Gaussian kernel of 12° SD. These tuning curves estimate how sharply each cell was tuned to the internal HD state inferred from population activity. In contrast, conventional real HD tuning curves estimate tuning relative to the animal's measured HD in the external environment. Real HD tuning curves used for comparison with manifold tuning curves were computed by downsampling real HD into 200 ms bins and applying the same procedure as above.

Statistics and reproducibility

All analyses were conducted using Matlab R2020b (Mathworks) with TStoolbox (https://github.com/PeyracheLab/TStoolbox) and Circular Statistics Toolbox version 1.2167[81]. Statistical comparisons of individual cell data were performed using a generalized linear mixed model (GLMM) approach[82] in order to take into account the hierarchy of dependency in our data sets (genotypes-rats-neurons) and account for random effects. Statistical modelling routines for the LME models were written and run using RStudio 2023.12 (RStudio Team). Depending on the data distribution (normal, lognormal or gamma), linear mixed models or GLMMs were fitted to single unit data metrics using the R package lme4 v1.1–17. Animal and cell identity were included in models as random effects, and genotypes and age cohort (where appropriate) were included as fixed effects. Where relevant, models additionally included angular head velocity, linear velocity, and

percentage time facing the cue as fixed-effect covariates. The *p*-values reported in the context of LMEs are given by likelihood ratio tests between a model containing the variable or interaction in question and a model without that variable or interaction (a reduced/null model). As an additional sensitivity analysis, statistically significant LME effects were also examined using non-parametric tests on cell-level values. These tests led to the same qualitative conclusions.

Statistical comparisons on animal averages (where stated) were performed with independent or paired Student's *t*-tests. All statistical tests were two-tailed. No statistical methods were used to pre-determine sample sizes, but our sample sizes are similar to those reported in previous publications.

Statistical analyses were based on planned comparisons targeting two main properties of the HD representation: tuning precision and drift relative to the external reference frame. HD information and tuning curve offset were used as primary measures, with tuning width, resultant vector length, decoding drift, and manifold-derived tuning used as complementary readouts. Because these measures addressed predefined questions rather than independent exploratory tests, no single correction was applied across all comparisons. Exact *p*-values, effect estimates, confidence intervals, and sample sizes are reported throughout.

Reporting summary

Further information on research design is available in the Nature Portfolio Reporting Summary linked to this article.

Data availability

All data used in this study, including extracellular electrophysiological recordings from the postsubiculum (spike times, spike waveforms and local field potentials), behavioural tracking data (position and head direction) and sleep state annotations are publicly available in the DANDI Archive[83] under Dandiset ID 001699 at https://dandiarchive.org/dandiset/001699 with https://doi.org/10.48324/dandi.001699/0.260917.2322. The source data for the main figures is in Supplementary Data 1.

Code availability

The code generated is available at the following address: https://doi.org/10.6084/m9.figshare.33943282.

Received: 15 January 2026; Accepted: 6 October 2026;
Published online: 10 November 2026

References

1. Manoli, D. S. & State, M. W. Autism spectrum disorder genetics and the search for pathological mechanisms. *Am. J. Psychiatry* **178**, 30–38 (2021).
2. Möhrle, D. et al. What we can learn from a genetic rodent model about autism. *Neurosci. Biobehav. Rev.* **109**, 29–53 (2020).
3. Till, S. M. et al. Conserved hippocampal cellular pathophysiology but distinct behavioural deficits in a new rat model of FXS. *Hum. Mol. Genet.* **24**, 5977–5984 (2015).
4. Asiminas, A. et al. Sustained correction of associative learning deficits after brief, early treatment in a rat model of fragile X syndrome. *Sci. Transl. Med.* **11**, eaao0498 (2019).
5. Asiminas, A. et al. Experience-dependent changes in hippocampal spatial activity and hippocampal circuit function are disrupted in a rat model of fragile X syndrome. *Mol. Autism* **13**, 49 (2022).
6. Katsanevaki, D. et al. Heterozygous deletion of SYNGAP enzymatic domains in rats causes selective learning, social and seizure phenotypes. Preprint at *bioRxiv* https://doi.org/10.1101/2020.10.14.339192 (2020).
7. Katsanevaki, D. et al. Key roles of C2/GAP domains in SYNGAP1-related pathophysiology. *Cell Rep.* **43**, 114733 (2024).
8. Klibaite, U. et al. Mapping the landscape of social behavior. *Cell* **188**, 2249–2266 (2025).
9. Lim, H. K., Yoon, J. H. & Song, M. Autism spectrum disorder genes: disease-related networks and compensatory strategies. *Front. Mol. Neurosci.* **15**, 922840 (2022).
10. Booker, S. A. et al. Altered dendritic spine function and integration in a mouse model of fragile X syndrome. *Nat. Commun.* **10**, 4813 (2019).
11. Domanski, A. P. F., Booker, S. A., Wyllie, D. J. A., Isaac, J. T. R. & Kind, P. C. Cellular and synaptic phenotypes lead to disrupted information processing in Fmr1-KO mouse layer 4 barrel cortex. *Nat. Commun.* **10**, 4814 (2019).
12. Raspanti, A. et al. Postnatal sensory experience and barrel cortex alterations anticipate autistic traits in a mouse model of Cdkl5 deficiency disorder. Preprint at *bioRxiv* https://doi.org/10.1101/2024.12.20.629347 (2024).
13. Fagiolini, M., Pizzorusso, T., Berardi, N., Domenici, L. & Maffei, L. Functional postnatal development of the rat primary visual cortex and the role of visual experience: dark rearing and monocular deprivation. *Vision Res.* **34**, 709–720 (1994).
14. Mitrukhina, O., Suchkov, D., Khazipov, R. & Minlebaev, M. Imprecise whisker map in the neonatal rat barrel cortex. *Cereb. Cortex* **25**, 3458–3467 (2015).
15. Che, A. et al. Layer I interneurons sharpen sensory maps during neonatal development. *Neuron* **99**, 98–116.e7 (2018).
16. Ames, C. & Fletcher-Watson, S. A review of methods in the study of attention in autism. *Dev. Rev.* **30**, 52–73 (2010).
17. Robertson, C. E. & Baron-Cohen, S. Sensory perception in autism. *Nat. Rev. Neurosci.* **18**, 671–684 (2017).
18. McNaughton, B. L., Battaglia, F. P., Jensen, O., Moser, E. I. & Moser, M.-B. Path integration and the neural basis of the 'cognitive map'. *Nat. Rev. Neurosci.* **7**, 663–678 (2006).
19. Langston, R. F. et al. Development of the spatial representation system in the rat. *Science* https://www.science.org/doi/abs/10.1126/science.1188210 (2010).
20. Wills, T. J., Cacucci, F., Burgess, N. & O'Keefe, J. Development of the hippocampal cognitive map in preweanling rats. *Science* **328**, 1573–1576 (2010).
21. Tan, H. M., Bassett, J. P., O'Keefe, J., Cacucci, F. & Wills, T. J. The development of the head direction system before eye opening in the rat. *Curr. Biol.* **25**, 479–483 (2015).
22. Bassett, J. P., Wills, T. J. & Cacucci, F. Self-organized attractor dynamics in the developing head direction circuit. *Curr. Biol.* **28**, 609–615.e3 (2018).
23. Chaudhuri, R., Gerçek, B., Pandey, B., Peyrache, A. & Fiete, I. The intrinsic attractor manifold and population dynamics of a canonical cognitive circuit across waking and sleep. *Nat. Neurosci.* **22**, 1512–1520 (2019).
24. Gardner, R. J. et al. Toroidal topology of population activity in grid cells. *Nature* **602**, 123–128 (2022).
25. Duszkiewicz, A. J. et al. Local origin of excitatory–inhibitory tuning equivalence in a cortical network. *Nat. Neurosci.* **27**, 782–792 (2024).
26. Hermansen, E., Klindt, D. A. & Dunn, B. A. Uncovering 2-D toroidal representations in grid cell ensemble activity during 1-D behavior. *Nat. Commun.* **15**, 5429 (2024).
27. Peng, J.-J. et al. Grid cells accurately track movement during path integration-based navigation despite switching reference frames. *Nat. Neurosci.* **28**, 2092–2105 (2025).
28. Peyrache, A., Lacroix, M. M., Petersen, P. C. & Buzsáki, G. Internally organized mechanisms of the head direction sense. *Nat. Neurosci.* **18**, 569–575 (2015).
29. Hunter, J. et al. Epidemiology of fragile X syndrome: a systematic review and meta-analysis. *Am. J. Med. Genet. A.* **164A**, 1648–1658 (2014).
30. Duszkiewicz, A. J., Fricker, D., Burgalossi, A. & Peyrache, A. The postsubiculum as a head-direction cortex. *Trends Neurosci.* **48**, 829–840 (2025).

31. Taube, J. S., Muller, R. U. & Ranck, J. B. Head-direction cells recorded from the postsubiculum in freely moving rats. I. Description and quantitative analysis. *J. Neurosci.* **10**, 420–435 (1990).
32. Viejo, G. & Peyrache, A. Precise coupling of the thalamic head-direction system to hippocampal ripples. *Nat. Commun.* **11**, 2524 (2020).
33. Mehrotra, D. et al. Hyperpolarization-activated currents drive neuronal activation sequences in sleep. *Curr. Biol. CB* **34**, 3043–3054.e8 (2024).
34. McCormick, D. A. & Prince, D. A. Post-natal development of electrophysiological properties of rat cerebral cortical pyramidal neurones. *J. Physiol.* **393**, 743–762 (1987).
35. Tian, Y. et al. Loss of FMRP impaired hippocampal long-term plasticity and spatial learning in rats. *Front. Mol. Neurosci.* **10**, 269 (2017).
36. Engineer, C. T. et al. Degraded speech sound processing in a rat model of fragile X syndrome. *Brain Res.* **1564**, 72–84 (2014).
37. Auerbach, B. D., Manohar, S., Radziwon, K. & Salvi, R. Auditory hypersensitivity and processing deficits in a rat model of fragile X syndrome. *Neurobiol. Dis.* **161**, 105541 (2021).
38. Berzhanskaya, J. et al. Disrupted cortical state regulation in a rat model of fragile X syndrome. *Cereb. Cortex* **27**, bhv331 (2017).
39. Kenkel, W. M. et al. Functional magnetic resonance imaging in awake transgenic fragile X rats: evidence of dysregulation in reward processing in the mesolimbic/habenular neural circuit. *Transl. Psychiatry* **6**, e763 (2016).
40. Taube, J. S. The head direction signal: origins and sensory-motor integration. *Annu. Rev. Neurosci.* **30**, 181–207 (2007).
41. Peyrache, A., Duszkiewicz, A. J., Viejo, G. & Angeles-Duran, S. Thalamocortical processing of the head-direction sense. *Prog. Neurobiol.* **183**, 101693 (2019).
42. Skaggs, W. E., Knierim, J. J., Kudrimoti, H. S. & McNaughton, B. L. A model of the neural basis of the rat's sense of direction. *Adv. Neural Inf. Process. Syst.* **7**, 173–180 (1995).
43. Redish, A. D., Elga, A. N. & Touretzky, D. S. A coupled attractor model of the rodent head direction system. *Netw. Comput. Neural Syst.* **7**, 671 (1996).
44. Sharp, P. E., Blair, H. T. & Cho, J. The anatomical and computational basis of the rat head-direction cell signal. *Trends Neurosci* **24**, 289–294 (2001).
45. Xie, X., Hahnloser, R. H. R. & Seung, H. S. Double-ring network model of the head-direction system. *Phys. Rev. E* **66**, 041902 (2002).
46. Blair, H. T., Cho, J. & Sharp, P. E. Role of the lateral mammillary nucleus in the rat head direction circuit: a combined single unit recording and lesion study. *Neuron* **21**, 1387–1397 (1998).
47. Bassett, J. P., Tullman, M. L. & Taube, J. S. Lesions of the tegmentomammillary circuit in the head direction system disrupt the head direction signal in the anterior thalamus. *J. Neurosci.* **27**, 7564–7577 (2007).
48. Senzai, Y. & Scanziani, M. A cognitive process occurring during sleep is revealed by rapid eye movements. *Science* **377**, 999–1004 (2022).
49. Asumbisa, K., Peyrache, A. & Trenholm, S. Flexible cue anchoring strategies enable stable head direction coding in both sighted and blind animals. *Nat. Commun.* **13**, 5483 (2022).
50. Skromne Carrasco, S., Viejo, G. & Peyrache, A. Months-long stability of the head-direction system. *Nature* **652**, 167–173 (2026).
51. Goodridge, J. P. & Taube, J. S. Interaction between the postsubiculum and anterior thalamus in the generation of head direction cell activity. *J. Neurosci.* **17**, 9315–9330 (1997).
52. Yoder, R. M., Clark, B. J. & Taube, J. S. Origins of landmark encoding in the brain. *Trends Neurosci.* **34**, 561–571 (2011).
53. Taube, J. S., Muller, R. U. & Ranck, J. B. Head-direction cells recorded from the postsubiculum in freely moving rats. II. Effects of environmental manipulations. *J. Neurosci.* **10**, 436–447 (1990).
54. Ajabi, Z., Keinath, A. T., Wei, X.-X. & Brandon, M. P. Population dynamics of head-direction neurons during drift and reorientation. *Nature* **615**, 892–899 (2023).
55. Krausse, S., Duszkiewicz, A. J., Neftci, E., Sommer, F. T. & Renner, A. Parallax error indicates simple cue-anchoring in the head-direction system. Preprint at *bioRxiv* https://doi.org/10.1101/2025.04.25.650191 (2026).
56. Siegenthaler, D. et al. Visual objects refine head direction coding. *Science* **389**, eadu9828 (2025).
57. Secer, G., Krishnan, B., Cowan, N. J. & Knierim, J. J. Visual landmark coding and dynamic coupling with path integration circuits in area 29e of the rodent parahippocampal cortex. Preprint at *bioRxiv* https://doi.org/10.1101/2025.11.11.687899 (2025).
58. Jacob, P.-Y. et al. An independent, landmark-dominated head-direction signal in dysgranular retrosplenial cortex. *Nat. Neurosci.* **20**, 173–175 (2017).
59. Sit, K. K. & Goard, M. J. Coregistration of heading to visual cues in retrosplenial cortex. *Nat. Commun.* **14**, 1992 (2023).
60. Poljac, E., Hoofs, V., Princen, M. M. & Poljac, E. Understanding behavioural rigidity in autism spectrum conditions: the role of intentional control. *J. Autism Dev. Disord.* **47**, 714–727 (2017).
61. Watanabe, T., Lawson, R. P., Walldén, Y. S. E. & Rees, G. A neuroanatomical substrate linking perceptual stability to cognitive rigidity in autism. *J. Neurosci.* **39**, 6540–6554 (2019).
62. Petrolini, V., Jorba, M. & Vicente, A. What does it take to be rigid? Reflections on the notion of rigidity in autism. *Front. Psychiatry* **14**, 1072362 (2023).
63. Booker, S. A. et al. Input-output relationship of CA1 pyramidal neurons reveals intact homeostatic mechanisms in a mouse model of fragile X syndrome. *Cell Rep.* **32**, 107988 (2020).
64. Liu, X., Kumar, V., Tsai, N.-P. & Auerbach, B. D. Hyperexcitability and homeostasis in fragile X syndrome. *Front. Mol. Neurosci.* **14**, 805929 (2022).
65. Berzhanskaya, J., Phillips, M. A., Shen, J. & Colonnese, M. T. Sensory hypo-excitability in a rat model of fetal development in fragile X Syndrome. *Sci. Rep.* **6**, 30769 (2016).
66. Rogers, S. J. Developmental regression in autism spectrum disorders. *Ment. Retard. Dev. Disabil. Res. Rev.* **10**, 139–143 (2004).
67. Frank, M. G. & Heller, H. C. Development of REM and slow wave sleep in the rat. *Am. J. Physiol.-Regul. Integr. Comp. Physiol.* **272**, R1792–R1799 (1997).
68. Rasch, B. & Born, J. About sleep's role in memory. *Physiol. Rev.* **93**, 681–766 (2013).
69. Marks, G. A., Shaffery, J. P., Oksenberg, A., Speciale, S. G. & Roffwarg, H. P. A functional role for REM sleep in brain maturation. *Behav. Brain Res.* **69**, 1–11 (1995).
70. Li, W., Ma, L., Yang, G. & Gan, W.-B. REM sleep selectively prunes and maintains new synapses in development and learning. *Nat. Neurosci.* **20**, 427–437 (2017).
71. Corner, M. A. et al. Does rapid-eye-movement sleep play a role in brain development? *Prog. Brain Res.* **53**, 347–356 (1980).
72. Mirmiran, M. et al. Effects of experimental suppression of active (REM) sleep during early development upon adult brain and behavior in the rat. *Dev. Brain Res.* **7**, 277–286 (1983).
73. Saré, R. M. et al. Deficient sleep in mouse models of fragile X syndrome. *Front. Mol. Neurosci.* **10**, 280 (2017).
74. Wang, H.-B. et al. Scheduled feeding improves behavioral outcomes and reduces inflammation in a mouse model of fragile X syndrome. *eLife* **14**, RP104720 (2025).
75. Miano, S. et al. Sleep phenotypes of intellectual disability: a polysomnographic evaluation in subjects with Down syndrome and fragile-X syndrome. *Clin. Neurophysiol.* **119**, 1242–1247 (2008).
76. Kronk, R. et al. Prevalence, nature, and correlates of sleep problems among children with fragile X syndrome based on a large scale parent survey. *Sleep* **33**, 679–687 (2010).

77. Lopes, G. et al. Bonsai: an event-based framework for processing and controlling data streams. *Front. Neuroinformatics* **9**, 7 (2015).
78. Zhang, K., Ginzburg, I., McNaughton, B. L. & Sejnowski, T. J. Interpreting neuronal population activity by reconstruction: unified framework with application to hippocampal place cells. *J. Neurophysiol.* **79**, 1017–1044 (1998).
79. Watson, B. O., Levenstein, D., Greene, J. P., Gelinas, J. N. & Buzsáki, G. Network homeostasis and state dynamics of neocortical sleep. *Neuron* **90**, 839–852 (2016).
80. Levenstein, D., Buzsáki, G. & Rinzel, J. NREM sleep in the rodent neocortex and hippocampus reflects excitable dynamics. *Nat. Commun.* **10**, 2478 (2019).
81. Berens, P. CircStat: a MATLAB toolbox for circular statistics. *J. Stat. Softw.* **31**, 1–21 (2009).
82. Yu, Z. et al. Beyond t test and ANOVA: applications of mixed-effects models for more rigorous statistical analysis in neuroscience research. *Neuron* **110**, 21–35 (2022).
83. Moore, N. et al. Age-dependent alterations in the head-direction signal in a rat model of fragile X syndrome. *DANDI Archive* https://doi.org/10.48324/DANDI.001699/0.260917.2313.

Acknowledgements

The authors thank Lynn Morrison and the other animal technicians from the University of Edinburgh George Square BioVeterinary Services Facility for their expertise & assistance in this work, and Dr Owen Dando for help implementing the LME analysis.

Author contributions

Conceptualization: A.J.D., A.P., E.R.W.; Methodology: P.A.D., A.J.D., N.M., A.P., E.R.W.; Software: A.J.D, N.M., A.P.; Validation: A.J.D, N.M.; Formal analysis: A.J.D., N.M.; Investigation: A.J.D., N.M.; Resources: A.A., A.J.D., N.M. Data curation: A.J.D., N.M.; Writing–original draft preparation: A.J.D.; Writing–review & editing: A.A., P.A.D., A.J.D., N.M., A.P., E.R.W.; Visualization: A.J.D.; Supervision: A.J.D., A.P., E.R.W.; Project administration: Wood A.J.D., A.P., E.R.W.; Funding acquisition: A.J.D., A.P., E.R.W.

Funding

N.M. was supported by a PhD studentship from the Simons Initiative for the Developing Brain. This work was supported by pilot funding from the Edinburgh-McGill pilot funding scheme (A.P., E.R.W.), and from the Simons Initiative for the Developing Brain (E.R.W. & A.A.), the Simons Foundation Autism Research Initiative grant AN-AR-Rat Models-0090333 (A.J.D., P.A.D., and A.P.), the Canadian Research Chair in Systems Neuroscience (A.P.), CIHR Project Grants 155957 and 180330 (A.P.); NSERC Discovery Grant RGPIN-2018-04600 (A.P.).

Competing interests

The authors declare no competing interests.

Additional information

Supplementary information The online version contains supplementary material available at https://doi.org/10.1038/s42003-026-11197-6.

Correspondence and requests for materials should be addressed to Adrian J. Duszkiewicz, Adrien Peyrache or Emma R. Wood.

Peer review information *Communications Biology* thanks all reviewer(s) for their contribution to the peer review of this work. Primary Handling Editors: Jasmine Pan.

Reprints and permissions information is available at http://www.nature.com/reprints

Publisher's note Springer Nature remains neutral with regard to jurisdictional claims in published maps and institutional affiliations.

Open Access This article is licensed under a Creative Commons Attribution 4.0 International License, which permits use, sharing, adaptation, distribution and reproduction in any medium or format, as long as you give appropriate credit to the original author(s) and the source, provide a link to the Creative Commons licence, and indicate if changes were made. The images or other third party material in this article are included in the article's Creative Commons licence, unless indicated otherwise in a credit line to the material. If material is not included in the article's Creative Commons licence and your intended use is not permitted by statutory regulation or exceeds the permitted use, you will need to obtain permission directly from the copyright holder. To view a copy of this licence, visit http://creativecommons.org/licenses/by/4.0/.

© The Author(s) 2026

This Article in Press is shared early to give you faster access to new research. It is citable and carries a permanent DOI. The final edited version will replace it automatically.